Journal of Petroleum Science and Engineering 187 (2020) 106788

Contents lists available at ScienceDirect

Journal of Petroleum Science and Engineering

journal homepage: http://www.elsevier.com/locate/petrol

Hydrocyclone for oil-water separations with high oil content: Comparison between CFD simulations and experimental data

C.A.O. de Araújo [a,*], C.M. Scheid [b], J.B.R. Loureiro [c], T.S. Klein [a], R.A. Medronho [a]

[a] Federal University of Rio de Janeiro/School of Chemistry/Chemical Engineering Department, Center of Technology, 21941-909, Rio de Janeiro, RJ, Brazil
[b] Federal Rural University of Rio de Janeiro/Institute of Technology/Chemical Engineering Department, 23890-000, Seropédica, RJ, Brazil
[c] Federal University of Rio de Janeiro/Mechanical Engineering Department (DEM/Poli/UFRJ), C.P. 68526, 21941-972, Rio de Janeiro, RJ, Brazil

ARTICLE INFO

Keywords:
Hydrocyclones
Oil-water separation
Computational fluid dynamics
Particle image velocimetry
Factorial design
CFD
PIV

ABSTRACT

Production separators for gas-oil-water separation are huge, require long residence times, and present several internals to improve oil-water separation. As an alternative to production separators, specially for subsea facilities, this work presents a hydrocyclone which separates a 40% oil-in-water mixture with 93% ± 2% total efficiency and flow ratio of 7%. Such high oil concentration is typical of mature wells and hydrocyclones have not been designed for such purpose before. In order to design this hydrocyclone, fractional factorial techniques have been used to consider the influence of seven geometrical variables. CFD has been used to assess the performance of each hydrocyclone of the factorial design. The selected hydrocyclone has been tested experimentally in order to validate its performance. PIV measurements have also been carried out in order to assess tangential and axial mean velocity profiles for only water flowing in the hydrocyclone. FBRM has been used to measure droplet size distribution at inlet, overflow and underflow streams. As results, computational reduced total efficiency has been experimentally confirmed. Numerical simulations captured tangential velocity near the centerline of the hydrocyclone, but failed in predicting axial velocity profiles and tangential velocity peaks and near wall regions. It has been discussed though that these are probably not responsible for oil droplets separation in the hydrocyclone when water is the continuous phase. A methodology to analyze the effect of droplet breakup and coalescence, using measured inlet, overflow and underflow cumulative size distribution, has been presented. It has been shown that for the inlet cumulative undersize distribution used, breakup was negligible and coalescence occurred only for droplet diameters higher than those separated with 100% grade efficiency. In this case, no breakup and coalescence models are thus needed in the mathematical model and this explains why reduced total efficiency has matched in both numerical simulations and experiments.

1. Introduction

Hydrocyclones are low-cost, compact equipment originally developed for solid-liquid separation, but currently also used for solid-solid, liquid-liquid and gas-liquid separation. The first patent dates from the late nineteenth century (Bretney, 1891) and its use has been intensified in the mid 1940s in the mining industry. According to Young et al. (1994), in the 1980s, hydrocyclones were first used to clean oil from offshore produced brine and since then they have been used as de-oiling devices. Due to advantages like low costs, high separation efficiency, low energy consumption and small space required, hydrocyclones are widely applied in various field such as mineral (Zhang et al., 2017), petroleum (Rocha et al., 2017), environmental (Liu et al., 2017; Ni et al., 2016), chemical (Cao et al., 2016) and food engineering (Altieri et al., 2015).

Classic hydrocyclones consist of a cylindrical part coupled to a conical section. A tangential inlet is placed at the upper part of the cylindrical section and there are two outlets: the top outlet, referred to as the overflow, and the bottom outlet, at the end of the conical part, referred to as the underflow. The overflow has a higher content of the less dense phase while the underflow collects the heaviest phase. The development of this geometry for oil-water separation led to a configuration based on two opposed inlets and two conic sections to increase separation efficiency. Fig. 1 shows a sketch of a hydrocyclone for oil-water separation, with its main geometrical characteristics indicated.

The literature often reports the usage of hydrocyclones for oil-water

* Corresponding author.
E-mail address: cristianoagenor@ufvjm.edu.br (C.A.O. de Araújo).

https://doi.org/10.1016/j.petrol.2019.106788
Received 11 May 2019; Received in revised form 31 October 2019; Accepted 5 December 2019
Available online 10 December 2019

separation for low compositions of the oil phase (Liu et al., 2019; Huang et al., 2018; Huang et al., 2017; Bai et al., 2011; Zhou et al., 2010). This is probably due to their successful first application in the oil industry as de-oiling devices (Young et al., 1994) to treat produced water. In such cases, oil concentration ranges from 40 mg/L up to 3%. High efficiencies such as 92% can be achieved (Huang et al., 2018), however separation efficiencies range on average between 40% and 80% (Bai et al., 2011; Motin et al., 2017).

Hamza et al. (2019) have investigated separation efficiency in a hydrocyclone for higher oil concentrations than usual to be applied in mature oil fields. They have assessed oil-in-water concentrations of 10%, 20% and 30% with mean droplet size at inlet of 37 μm and separation efficiencies have been reported to be of 84% maximum. Liu et al. (2018) have also worked with oil-in-water concentrations of 10% and have reported efficiencies from 86 to 92%.

With regard to the design of hydrocyclones for oil-water separation, it used to be based on empirical relations and/or scale-up procedures for geometrically similar hydrocyclones (Medronho and Svarovsky, 1984; Antunes and Medronho, 1992; Castilho and Medronho, 2000; Coelho and Medronho, 2001), in spite of the limited use of most empirical relations available (since these had been developed solely for solid-liquid separation). Therefore, experiments used to be (and at some point still are) typically required to validate and sometimes design and optimize hydrocyclones for particular purposes. For instance, experimental techniques, such as factorial design, have been successfully applied to study the effect of geometric and operational variables on the separation efficiency of hydrocyclones (Obeng et al., 2005; Elsayed and Lacor, 2010; Braga et al., 2015).

Due to the complex internal flow field in hydrocyclones, Computational Fluid Dynamics (CFD) has been used to improve flow field understanding as well as for design and geometry optimization of hydrocyclones (Liu et al., 2019; Wang and Wu, 2018; Braga et al., 2015; Elsayed and Lacor, 2010; Schütz et al., 2009). Most of such numerical simulations are commonly combined with experiments for validation.

The present work uses CFD, fractional factorial design and experimental techniques in order to determine a geometry of a hydrocyclone for oil-water separation with high oil concentration, such as 40%, yet not reported in the literature. Such high concentration is typical of produced mature well fluid.

Typical offshore platforms first separate oil from water with production separators, which are huge, therefore demanding high floor space and requiring long residence times, and can be very complex inside due to internals to improve separation. These characteristics of production separators make them expensive in the process. The motivation of the present work is thus to design a hydrocyclone to be an alternative to production separators as a whole, but specially for subsea facilities, where definitely, the simpler the equipment, the best.

2. Methodology

2.1. Fractional factorial design

In order to achieve a hydrocyclone capable of separating high levels of oil from water, experimental design techniques have been used. Since many geometric variables are known to influence the separation efficiency in hydrocyclones, the fractional factorial design method, which is a screening design technique meant to screen linear terms, has been used to provide a reduced number of experiments.

Instead of building different hydrocyclones and carrying out physical experiments to calculate separation efficiency and flow ratio, which would lead to high costs and long execution times, each experiment suggested by the fractional factorial design plan have been computationally tested using CFD.

A 2^{7-3} fractional factorial design has been performed in order to evaluate the main effect of seven geometrical variables, with two values each, on both separation efficiency and flow ratio.

Dimensions of each geometric variable shown in Fig. 1 have been chosen based on the experience of the current research group. The diameter of the cylindrical part, Dc, and the diameter between the first and second conical parts, D, have been kept constant and equal to 70 mm and 40 mm respectively. The geometric variables under study, as well as their lower and upper values considered in the present work, are presented in Table 1.

The *software* Design Expert® (version 6.0, StatEase) has been used to determine how many and which computational experiments should be carried out. Seventeen computational experiments have been suggested, the last being at the center point. As in the present work the experiments are carried out computationally, there is no reason to perform repetitions at the center point.

The outcome variables of interest for the fractional factorial design are: the reduced grade efficiency (G') and the flow ratio (R_F). The flow ratio is defined by:

$$R_F = \frac{W_{ac}}{W_a} \tag{1}$$

where W_{ac} is the water mass flow in the concentrated stream (overflow) and W_a is the water mass flow in the feed stream.

There is also the global flow ratio (also known as overflow-to-throughput ratio), R_{FT}, which is based on the total liquid flow at the inlet and outlet streams from the equipment, defined by:

$$R_{FT} = \frac{(Q_A + Q_O)_{overflow}}{(Q_A + Q_O)_{inlet}} \tag{2}$$

Table 1
Lower and upper values of the seven geometrical variables, described in Fig. 1, used in the fractional factorial design.

Variable	Lower value	Upper value
Do (mm)	5	20
Du (mm)	10	25
Di (mm)	7,5	17,5
VF (mm)	4	40
L1 (mm)	25	45
Θ_1 (degree)	5°	15°
Θ_2 (degree)	2°	15°

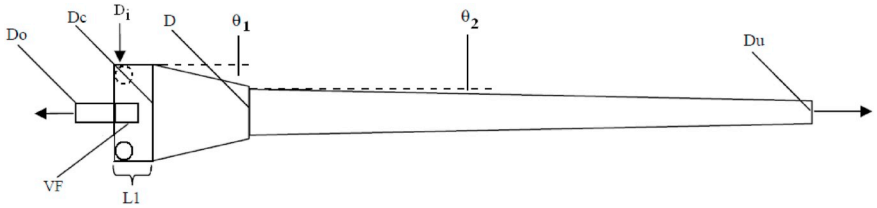

Fig. 1. Main geometric variables of a hydrocyclone for oil-water separation: overflow tube diameter, Do; underflow diameter, Du; feed tube diameter, Di; vortex finder length, VF; cylindrical part diameter, Dc; cylindrical section length, L1; diameter between the first and second conical parts, D; angle of the first conical section, Θ_1; and angle of the second conical section, Θ_2.

where Q_A is the water volumetric flow rate and Q_O is the oil volumetric flow rate.

The reduced grade efficiency G' can be obtained from the following expression:

$$G' = \frac{G - R_F}{1 - R_F} \tag{3}$$

where G is the grade efficiency:

$$G = \frac{W_{dc}}{W_d} \tag{4}$$

where W_{dc} is the mass flow of particles (or droplet) with size d in the concentrate stream and W_d is the mass flow of particles with size d in the feed stream. The same definition presented for the grade efficiency G and G' is applied to the total efficiency (E_T) and reduced efficiency (E_T'), respectively. The difference is that the grade efficiency corresponds to one particle size only, while the total efficiency is applied globally to all particles. Taking W as the total mass flow of particles (at inlet) and W_c the total mass flow of particles in the concentrate stream, E_T and E'_T are given by Equations (5) and (6) respectively.

$$E_T = \frac{W_c}{W} \tag{5}$$

$$E'_T = \frac{E_T - R_F}{1 - R_F} \tag{6}$$

The reduced grade efficiency G' is often expressed through the empirical relation suggested by Plitt (1976), where d'_{50}, is the reduced cutoff diameter, which represents the particle diameter which is separated with 50% reduced grade efficiency, and n is a parameter of the model:

$$G' = 1 - \exp\left[-0,693\left(\frac{d}{d'_{50}}\right)^n \right] \tag{7}$$

The reduced total efficiency can be also obtained by integrating the grade efficiency over all diameter sizes, through cumulative undersize distributions, $y(d)$. Hence, reduced total efficiency E'_T can be also calculated through Equation (8).

$$E'_T = \int_0^1 G' dy \tag{8}$$

Cumulative undersize distribution y is commonly related to particle (droplet) diameter d through the model proposed by Rosin and Rammler (1933), presented in Equation (9), where k and m are model parameters.

$$y = 1 - \exp\left[-\left(\frac{d}{k}\right)^m \right] \tag{9}$$

A mass balance for particles smaller than a given diameter provides a relation between the total efficiency E_T and the cumulative undersize distributions at inlet, y_i, and at the concentrated, y_o, and diluted, y_u, outlet streams, which is presented in Equation (10).

$$E_T = \frac{y_u - y_i}{y_u - y_o} \tag{10}$$

2.2. CFD simulations

Hexahedral meshes were built in ANSYS ICEM and grid independence tests have been carried out for the central point geometry to ensure grid-independent results. Further on, the same pattern has been replicated to build the meshes of the other hydrocyclones of the fractional factorial design plan. Grid independence was achieved for the central point hydrocyclone with around 400.000 elements. No significant differences for tangential velocity profiles at four different axial positions has been found when compared to a grid with 600.000 elements.

Fig. 2 shows the hexahedral mesh for the selected hydrocyclone which has 444.000 elements and presents maximum aspect ratio of 80, maximum volume change of 12, minimum orthogonal quality of 0.37, minimum determinant of 0.39 and minimum angle of 18.7°. This indicates the mesh is appropriate since aspect ratio should be less than 100, volume change should be smaller than 20, orthogonal quality should be greater than 0.15, determinant should be less than 0.2 and angle should be greater than 18° (ANSYS Meshing, 2010).

Simulations have been carried out in ANSYS FLUENT 13. In all of them the oil concentration at the inlet was kept at 40% (v/v) and an uniform velocity profile of 4 m/s has been set. Both overflow and underflow have been set with output pressure of 1 bar. The remained boundaries have been specified as wall with no slip condition.

Designing the hydrocyclone to operate with the same outlet pressures at the overflow and underflow should avoid the need of control valves to artificially change global flow ratio (R_{FT}) to improve in site separation efficiency.

The simulations carried out according to the fractional factorial design considered the oil droplet size as uniform and equal to 250 μm. In order to build the computational reduced grade efficiency curve for the hydrocyclone which performed best, several simulations have been carried out, varying the oil droplet size from 5 to 150 μm, which has been kept as uniform in each simulation. This allowed to determine the reduced cutoff droplet size of the selected hydrocyclone according to the CFD simulations.

The physical properties of the water and oil can be seen in Table 2.

Simulations used the pressure-based solver, the SIMPLE algorithm for pressure-velocity coupling and a second order upwind advection scheme. Numerical results have been considered converged when mean residuals RMS reached 10^{-5}. Simulations related to the fractional factorial design and those performed to build the reduced grade efficiency curve have been carried out in steady state. The hydrocyclone selected from the fractional factorial design has been also simulated in transient regime, for twelve seconds with a time step of 10^{-4}s. Both continuous and disperse phases, water and oil respectively, have been modeled according to the Eulerian approach. For the present case, the governing phase-averaged continuity and momentum equations are given by:

$$\frac{\partial}{\partial t}\left(\overline{\alpha_q}\rho_q\right) + \nabla.\left(\overline{\alpha_q}\rho_q\tilde{U}_q\right) = 0 \tag{11}$$

$$\frac{\partial}{\partial t}\left(\overline{\alpha_q}\rho_q\tilde{U}_q\right) + \nabla.\left(\overline{\alpha_q}\rho_q\tilde{U}_q\tilde{U}_q\right) = -\overline{\alpha_q}\nabla\tilde{p} + \nabla.\tilde{\tau}_q + \sum_{p=1}^{n} K_{pq}\left(\tilde{U}_p - \tilde{U}_q\right) \tag{12}$$

where q stands for the qth phase, α is the volume fraction, overbar denotes time-averaged values and tilde denotes phase-average variables, defined for a generic variable Φ_q as:

$$\tilde{\varphi}_q = \frac{\overline{\alpha_q \Phi_q}}{\overline{\alpha_q}} \tag{13}$$

The last term in the right-hand side of Equation (12) stands for the drag force and K_{pq} is the interphase momentum exchange coefficient between phases p and q, taken as in Equation (14), where f is the drag function, modeled according to Schiller and Naumann (1935) and presented in Equations (15) and (16).

$$K_{pq} = \frac{18\alpha_p(1-\alpha_p)\mu_q}{d_p^2} f \tag{14}$$

$$f = \frac{C_D Re}{24} \tag{15}$$

$$C_D = \frac{24(1 + 0.15Re^{0.687})}{Re} \quad Re \le 1000 \; or \; C_D = 0.44 \; Re > 1000 \tag{16}$$

where C_D is de drag coefficient and d_p is the particle (droplet) diameter.

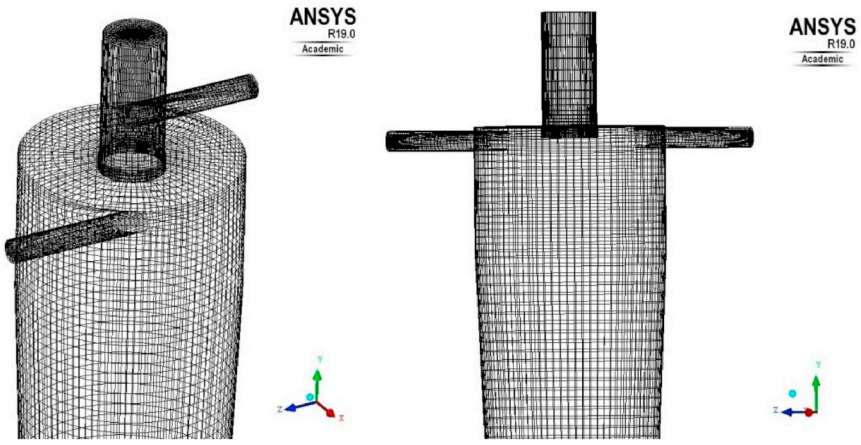

Fig. 2. Hexahedral mesh generated with ANSYS ICEM for the hydrocyclones of the present work.

Table 2
Physical properties of oil and water.

Material	Density (kg m^{-3})	Viscosity (kg m^{-1} s^{-1})
Water	996.5	0.855 10^{-3}
Oil	840	13.2 10^{-3}

Equations (15) and (16) depend on the relative Reynolds number *Re*, defined as:

$$Re = \frac{\rho_c |\tilde{U}_p - \tilde{U}_c| d_p}{\mu_c} \tag{17}$$

where *c* stands for the continuous phase and *p*, the dispersed phase (particles - droplets).

At last, the total phase-average stress-strain tensor of phase *q*, $\tilde{\tau}_q$ in Equation (12), accounts for both laminar and turbulent contributions:

$$\tilde{\tau}_q = \alpha_q \mu_q \left(\nabla \tilde{U}_q + \nabla \tilde{U}_q^T\right) - \overline{\alpha}_q \rho_q \tilde{R}_{ij} \tag{18}$$

It is assumed that the turbulence field is shared by all phases so mixture properties and mixture velocities, indicated by the subscript *m* and defined as in Equations (19) and (20), are used to compute the phase-average Reynolds stress tensor $\tilde{R}_{ij}$, which has been modeled according to the Reynolds stress model of Gibson and Launder (1978), presented in Equations (21)–(31) (ANSYS Fluent, 2010).

$$\Gamma_m = \sum_{i=1}^{N} \overline{\alpha}_i \Gamma_i \tag{19}$$

$$\tilde{U}_m = \frac{\sum_{i=1}^{N} \overline{\alpha}_i \rho_i \tilde{U}_i}{\sum_{i=1}^{N} \overline{\alpha}_i \rho_i} \tag{20}$$

$$\frac{\partial}{\partial t}\left(\rho_m \tilde{R}_{ij}\right) + \frac{\partial}{\partial x_k}\left(\rho_m \tilde{U}_k \tilde{R}_{ij}\right) = P_{ij} + \varphi_{ij} - \varepsilon_{ij} + D_{ij} \tag{21}$$

$$P_{ij} = -\rho_m \left(\tilde{R}_{ik}\frac{\partial \tilde{U}_j}{\partial x_k} + \tilde{R}_{jk}\frac{\partial \tilde{U}_i}{\partial x_k}\right) \tag{22}$$

$$\varphi_{ij} = \varphi_{ij,1} + \varphi_{ij,2} + \varphi_{ij,w1} + \varphi_{ij,w2} \tag{23}$$

$$\varphi_{ij,1} = -C_1 \rho_m \frac{\varepsilon}{k}\left[\tilde{R}_{ij} - \frac{2}{3}\delta_{ij} k\right] \tag{24}$$

$$\varphi_{ij,2} = -C_2 \left[\left(P_{ij} - \frac{2}{3}\delta_{ij}\frac{1}{2}P_{kk}\right)\right] \tag{25}$$

$$\varphi_{ij,w1} = C_1^{'}\frac{\varepsilon}{k}\left(\tilde{R}_{kl} n_k n_l \delta_{ij} - \frac{3}{2}\tilde{R}_{ik} n_j n_k - \frac{3}{2}\tilde{R}_{jk} n_i n_k\right)\frac{C_l k^{3/2}}{\varepsilon d} \tag{26}$$

$$\varphi_{ij,w2} = C_2^{'}\left(\varphi_{kl,2} n_k n_l \delta_{ij} - \frac{3}{2}\varphi_{ik,2} n_j n_k - \frac{3}{2}\varphi_{jk,2} n_i n_k\right)\frac{c_l k^{\frac{3}{2}}}{\varepsilon d} \tag{27}$$

$$\varepsilon_{ij} = \frac{3}{2}\delta_{ij}\rho_m \varepsilon \tag{28}$$

$$D_{ij} = \frac{\partial}{\partial x_k}\left[\left(\mu_m + \frac{\mu_{t,m}}{\sigma_k}\right)\frac{\partial \tilde{R}_{ij}}{\partial x_k}\right] \tag{29}$$

$$\mu_{t,m} = \rho_m C_\mu \frac{k^2}{\varepsilon} \tag{30}$$

$$\frac{\partial}{\partial t}(\rho_m \varepsilon) + \frac{\partial}{\partial x_k}(\rho_m u_k \varepsilon) = \frac{\partial}{\partial x_k}\left[\left(\mu_m + \frac{\mu_{t,m}}{\sigma_\varepsilon}\right)\frac{\partial \varepsilon}{\partial x_k}\right] + C_{\varepsilon 1}\frac{P_{ii}}{2}\frac{\varepsilon}{k} - C_{\varepsilon 2}\rho_m \frac{\varepsilon^2}{k} \tag{31}$$

In Equations (21)–(31), P_{ij} is the stress production term, φ_{ij} is the pressure strain term - modeled as a function of the slow pressure strain term $\varphi_{ij,1}$, the rapid pressure strain term $\varphi_{ij,2}$ and the wall reflection terms $\varphi_{ij,w1}$ *and* $\varphi_{ij,w2}$, ε_{ij} is the viscous dissipation term, D_{ij} is the total diffusion term, k is the turbulent kinetic energy, ε is its viscous dissipation rate, μ_t is the turbulent viscosity, n_k is the x_k component of the unit normal to the wall, d is the normal distance to the wall and the constants are as follow: $C_1 = 1.8$, $C_2 = 0.6$, $C'_1 = 0.5$, $C'_2 = 0.3$, $C_\ell = 0.3924$, $C_\mu = 0.09$, $C_{\varepsilon 1} = 1.44$, $C_{\varepsilon 2} = 1.92$, $\sigma_k = 1.0$ and $\sigma_\varepsilon = 1.0$.

2.3. Experimental setup

The most efficient hydrocyclone based on the fractional factorial design was built in acrylic and the same service which had been simulated was set up in order to validate the separation efficiency. Velocity fields have been measured with a PIV system to investigate the local flow behavior along the hydrocyclone. In addition, experimental mean velocity profiles have been compared with CFD simulation predictions in order to enrich the discussion of the results.

2.3.1. The PIV system

The PIV system was installed in a closed flow loop which operated solely with water as working fluid. The turbid oil phase was not added to this set of experiments, since it could block the laser lightsheet, preventing the proper illumination of the tracer particles. The experimental facility is presented in Fig. 3.

Three digital flow meters PRO 1000 (Incontrol) have been used at the two inlets and underflow streams. The pressure at the two inlets (P-1 and P-2, Fig. 3), overflow (P-3) and underflow (P-4) streams have been

measured by Bourdon gauges. Valves have been used to control the global flow ratio and a centrifugal pump CAM-W10 (Dancor, 2 hp) has been used to feed the hydrocyclone. The volumetric flow rate at inlet and global flow ratio have been adjusted to be 0.635 $m^3\ h^{-1}$ and 40% respectively, in accordance to the CFD simulations.

Measurements were performed with a LaVision 2D PIV system. The light source was provided by a Quantel BigSky double-pulsed Nd:YAG laser that furnished short duration (4 ns) and high energy (120 mJ) pulses of 532 nm wavelength. A series of cylindrical and spherical lenses were used to adjust the lightsheet thickness to 1 mm. The water flow was seed with fluorescent tracer particles in order avoid laser reflections either from the hydrocyclone walls or from gas bubbles that may appear on the vortex core, depending on the measurement conditions. The particles used had a density of 1190 kg m^{-3} and were made of PMMA (Poly methyl methacrylate) filled with Rhodamine 6G, which scatter light in the red wavelength. The PIV system used a 12 bit CCD camera with a resolution of 1376 × 1040 pixels, pixel size of 6.45 μm × 6.45 μm, fitted with an AF Micro-Nikkor 105 mm f/2.8D lens. A red filter was fitted to the camera lens to allow the entrance of wavelengths above 570 nm, blocking the green laser reflections. Davis Software 7.1 has been used for image processing.

The hydrocyclone was machined inside a solid rectangular acrylic box in order to avoid optical distortions of the flow. Uncertainty analysis of the measured mean velocity field has been calculated following the procedure recommend by Adrian (1997) and Coleman and Steele (2009). Contributions from random and bias uncertainty were taken into account. For the present experimental conditions, the highest overall uncertainty within 95% confidence interval was 0.06 m/s.

2.3.2. Oil-water open flow loop system

In order to measure separation efficiency, an oil-water open flow loop has been built, according to Fig. 4. The oil has been pumped with a positive displacement progressing cavity pump NEMO® (NETZSCH), which provides continuous pumping with low pulsation. Instead of the digital flow meters used in the water experiments, two AppliTech® rotameters have been used to measure flow rates of water and oil, since the formers do not work for mixtures containing high oil concentrations. The volumetric flow rates for the oil and water were 0.51 $m^3\ h^{-1}$ and 0.74 $m^3\ h^{-1}$ respectively.

This oil-water open rig has been used for three different, but complementary, purposes. The first and main purpose, as already mentioned, was to measure separation efficiency and flow ratio. The second, to measure droplet size distribution at inlet, overflow and underflow streams. The third, to assess how the global flow ratio R_{FT} (varied through the underflow valve) affects total efficiency.

In order to measure total separation efficiency and flow ratio and ensure reproducibility of the experimental procedure, three identical experiments have been performed with the same inlet flow rate and oil concentration of the two-phase CFD simulations.

The inline oil droplet size distribution has been measured with an FBRM. FBRM measures the real time (online) chord length (read as droplet size) distribution of the oil droplets through a focused beam reflectance measurement probe. The ParticleTrack of E25 (Metler Toledo), which has a fixed probe with 25 mm diameter and scan circle diameter of 5 mm, has been used.

Inlet droplet size distribution has been used to estimate reduced total efficiency according to the reduced grade efficiency curve obtained with CFD simulations. This allowed comparison between computational and experimental reduced total separation efficiency.

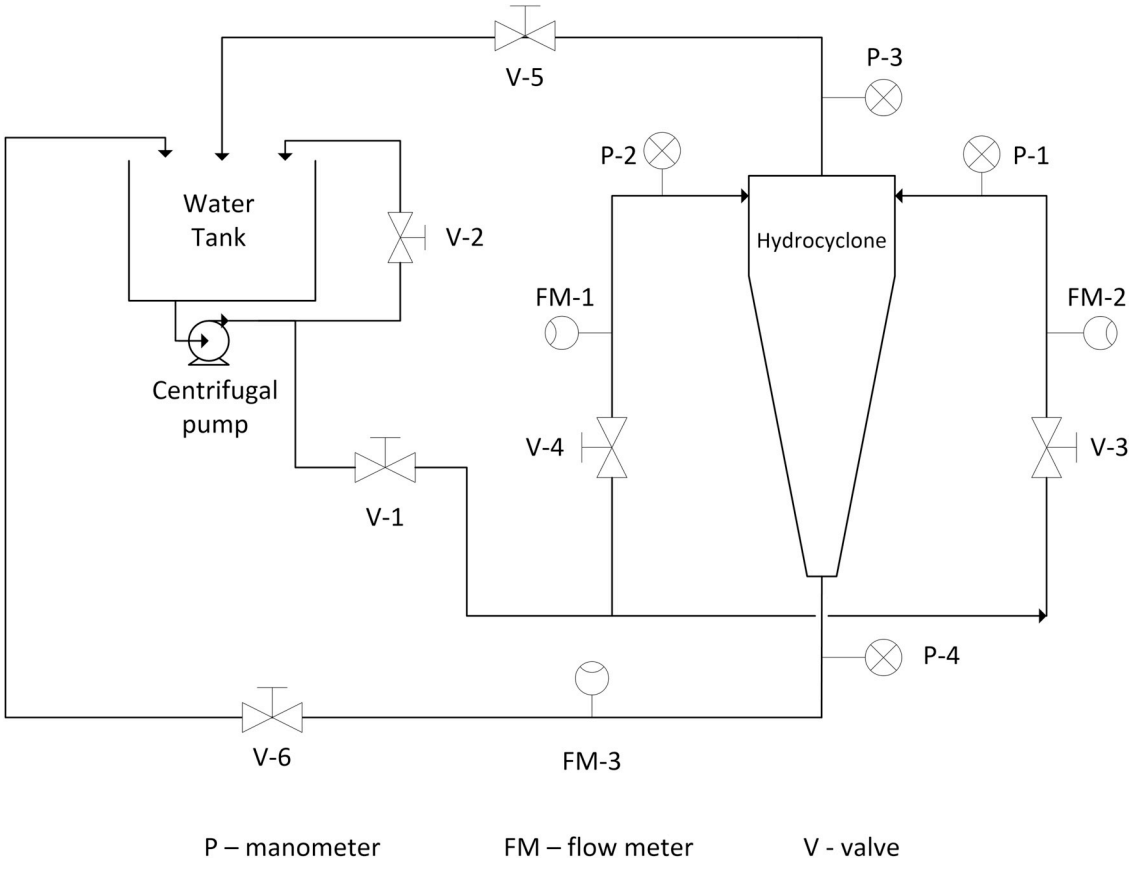

Fig. 3. Experimental setup of the closed flow loop PIV system to measure velocity profiles in the hydrocyclone.

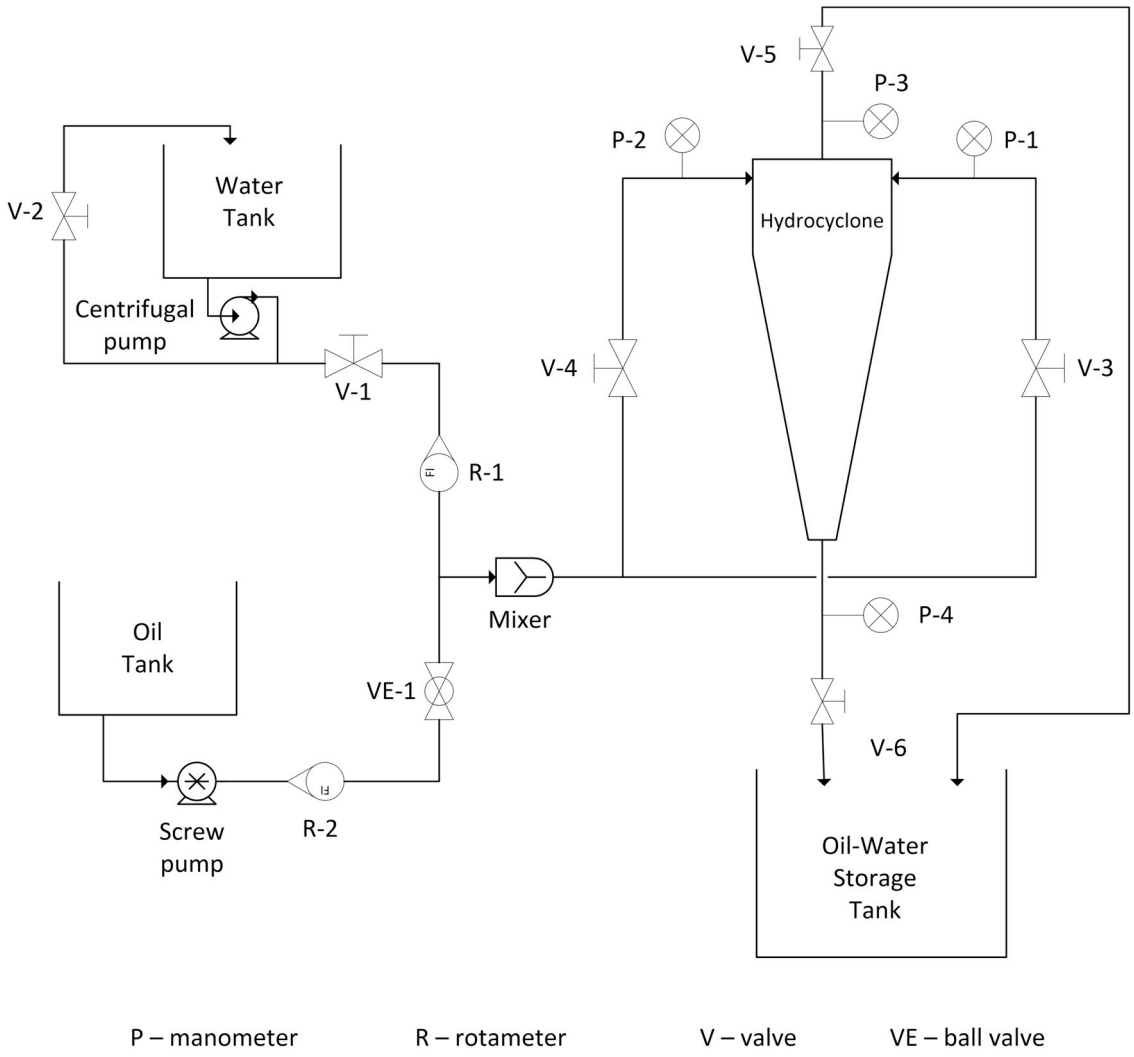

Fig. 4. Experimental setup of the open flow loop system to measure separation efficiency in the hydrocyclone.

3. Results and discussion

3.1. CFD simulations

Table 3 shows the values for all seven geometric variables suggested by the 2^{7-3} fractional factorial design and the values of grade efficiency (G') and flow ratio (R_F) obtained through the steady-state CFD simulations. These values refer to oil droplets of 250 μm of diameter.

The best hydrocyclone is the one which provides the highest grade efficiency and the lowest flow ratio. High values of R_F means that a large amount of water is leaving the hydrocyclone through the overflow stream, which is not of interest. Therefore the best hydrocyclones are

Table 3
Geometrical dimensions and the values of G' and R_F for the fractional factorial 2^{7-3} (screening) design, considering uniform droplets of 250 μm.

Simulation	Do (mm)	Du (mm)	VF (mm)	L1 (mm)	Θ_1 (rad)	Θ_2 (rad)	Di (mm)	R_f (%)	R_{FT} (%)	G (%)	G′(%)
1	5	10	4	25	0.0872	0.0349	7.5	0.40	13.90	34.25	33.95
2	20	10	4	25	0.2618	0.0349	17.5	62.20	77.30	99.99	99.97
3	5	25	4	25	0.2618	0.2618	7.5	0.00	0.00	0.00	0.00
4	20	25	4	25	0.0872	0.2618	17.5	1.80	21.20	50.41	49.50
5	5	10	40	25	0.2618	0.2618	17.5	8.50	11.90	17.13	9.42
6	20	10	40	25	0.0872	0.2618	7.5	94.40	95.90	97.63	57.92
7	5	25	40	25	0.0872	0.0349	17.5	0.00	0.00	0.00	0.00
8	20	25	40	25	0.2618	0.0349	7.5	1.00	38.50	94.93	94.87
9	5	10	4	45	0.0872	0.2618	17.5	0.00	16.54	41.37	41.36
10	20	10	4	45	0.2618	0.2618	7.5	100.00	100.00	100.00	(−)
11	5	25	4	45	0.2618	0.0349	17.5	0.00	0.00	0.00	0.00
12	20	25	4	45	0.0872	0.0349	7.5	3.51	41.96	99.66	99.64
13	5	10	40	45	0.2618	0.0349	7.5	4.60	10.90	20.35	16.50
14	20	10	40	45	0.0872	0.0349	17.5	58.20	74.90	99.96	99.92
15	5	25	40	45	0.0872	0.2618	7.5	0.40	1.10	2.10	1.67
16	20	25	40	45	0.2618	0.2618	17.5	10.32	21.10	39.31	32.33
17 (CP)	12.5	17.5	22	35	0.1745	0.1483	12.5	0.19	11.70	29.07	28.93

those of simulations 8 and 12 (HC-8 and HC-12). Since HC-12 has the highest grade efficiency and still a reasonably low flow ratio, it has been selected as the best hydrocyclone to be built in acrylic for experimental tests.

As mentioned above, CFD simulations of the HC-12 have also been investigated in transient regime. The values of R_F and G' obtained for the steady and unsteady states are presented in Table 4. The results are quite close, especially with regard to the grade efficiency. This confirms that steady state simulations are appropriate.

Fig. 5 shows the reduced grade efficiency curve for the HC-12 hydrocyclone obtained with CFD simulations. The reduced cutoff droplet size has then been obtained by fitting this curve into the linearized form of Equation (7), which provided $d'_{50} = 51.3$ μm, with a coefficient of determination (R^2) of 0.9978. It can be also noted in Fig. 5 that particles with diameters above 125 μm are collected with 100% reduced grade efficiency. The equation for the reduced grade efficiency curve obtained computationally for the HC-12 is then presented in Equation (32):

$$G' = 1 - \exp\left[-0.693\left(\frac{d}{51.3}\right)^{2.36}\right] \quad (32)$$

Equation (32) is a measure of the performance of the hydrocyclone HC-12, according to CFD simulations. It thus allows to estimate the computational reduced total efficiency for any inlet particle size distribution, according to Equation (10).

3.2. Velocity profiles obtained with PIV

Axial and tangential velocity profiles were measured at 300, 470 and 700 mm from the top of the HC-12 hydrocyclone, indicated by Stations 1 to 3 in Fig. 6. As mentioned before, these measurements have been taken with water as the only working fluid. CFD simulations have thus been carried out for water as single phase in order to compare the predicted velocity profiles with PIV measurements.

Fig. 7 compares tangential velocity profiles obtained with CFD simulations and experimentally with PIV. Tangential velocity is important because it is related to the centrifugal field within the equipment. This is the action that separates oil from water. Tangential velocity profiles have a similar shape inside the equipment. The shape of the velocity profiles found in this work are in agreement with other works (Huang et al., 2017; Huang et al., 2018; Zhen-bo et al., 2011; Noroozi and Hashemabadi, 2011; Marins et al., 2010; Dlamini et al., 2005; Slack et al., 2004). The magnitude of the tangential velocity increases as one moves from the central axis of the equipment towards the wall, in the radial direction, and reaches a peak. It then decreases until the no-slip condition is satisfied at the wall of the hydrocyclone.

The pioneering work of Kelsall (1952) on the measurement of velocity profiles in hydrocyclones have shown that the tangential velocity peak separates the forced and free vortex region, what has also been observed in the present work. The magnitude of the tangential velocity peak measured at each of the three Stations decreases as it approaches the underflow orifice, that is, as the diameter of the hydrocyclone decreases along the two conical sections.

It is possible to observe in Fig. 7a that CFD simulations have underpredicted tangential velocity profiles when compared to experimental data at Station 1. However, although CFD still underpredicts tangential velocity peaks and near wall region at Stations 2 and 3 (Fig. 7b and c respectively), numerical simulations slightly overpredict

Table 4
Results of CFD simulations of the HC-12 and oil droplet size of 250 μm in steady and unsteady states.

Regime	R_{FT} (%)	R_F (%)	G (%)	G' (%)
Steady State	41.96	3.51	99.66	99.64
Transient	41.23	2.25	99.77	99.77

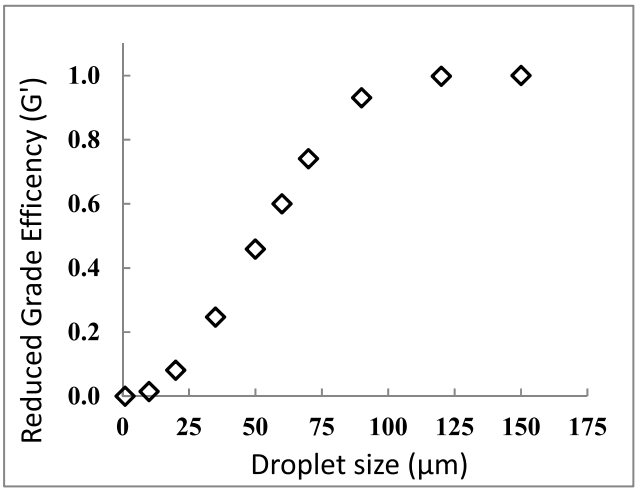

Fig. 5. Reduced grade efficiency curve for the HC-12, obtained with CFD simulations in steady state.

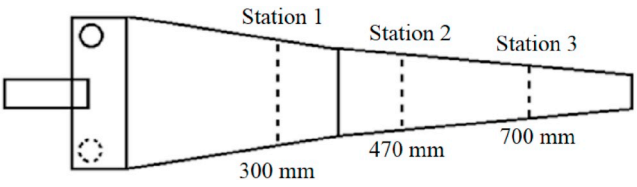

Fig. 6. Stations 1 to 3 where tangential and axial velocities have been measured.

tangential velocity magnitude close to the centerline of the hydrocyclone. As oil has lower density than water, the centrifugal field inside the hydrocyclone makes the oil migrate towards the central axis. Therefore, the tangential velocity profile in this region is expected to be mostly responsible for oil separation. As Fig. 7 refers to single phase simulation and experiment, these differences are related to the performance of the turbulence model used, which, in any way, is the most recommended for the complex flow inside the hydrocyclone. Nevertheless, as the region near the central axis is reasonably well predicted, this might not affect significantly the prediction of separation efficiency.

Fig. 8 compares axial velocity profiles obtained with CFD simulations and experimentally with PIV. It can be noted that while PIV measurements have provided an inverted "W" profile for all 3 axial positions, CFD simulations have predicted an inverted "V" profile at Stations 2 and 3. It should be noted that positive axial velocity values means liquid moving towards the overflow, while negative values means a downward movement at the central axis towards the underflow. At the central axis, where $r = 0$, PIV measurements provide very low velocities, close to zero, which means quasi-static flow.

This can be considered an unusual behavior. In general, the axial velocity is maximum at the centerline of the hydrocyclone, as seen in the CFD simulations for Stations 2 and 3 (Fig. 8b and c), and also in the work of Marins et al. (2010), Bhaskar et al. (2007), Swain and Mohanty (2013) and Saidi et al. (2012). These velocity peaks at the centerline of the equipment are usually high in magnitude close to the overflow region, reducing its intensity towards the underflow orifice. On the other hand, the inverted "W" axial velocity profile have also been reported by Murthy and Bhaskar (2012), Elsayed and Lacor (2010) and Harasek et al. (2008), who discussed the inverted "V" and "W" axial velocity profile obtained through experiments and also numerical simulations. Harasek et al. (2008) states that the physical reasons for the development of the inverted "V" and "W" shapes in the axial velocity profiles are still unknown. However, their experiments showed that the diameter of

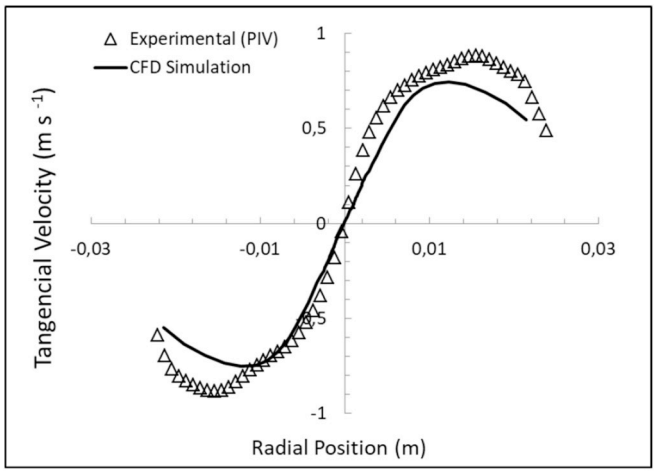

(a)

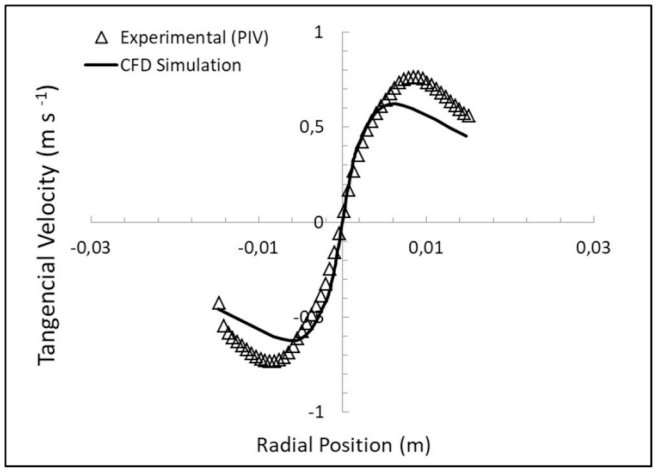

(b)

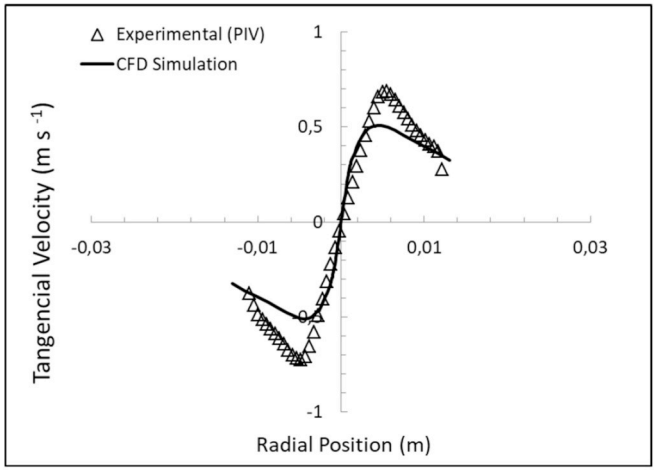

(c)

Fig. 7. Tangential velocity profiles from PIV and CFD simulations at (a) Station 1, (b) Station 2 and (c) Station 3, all indicated in Fig. 6.

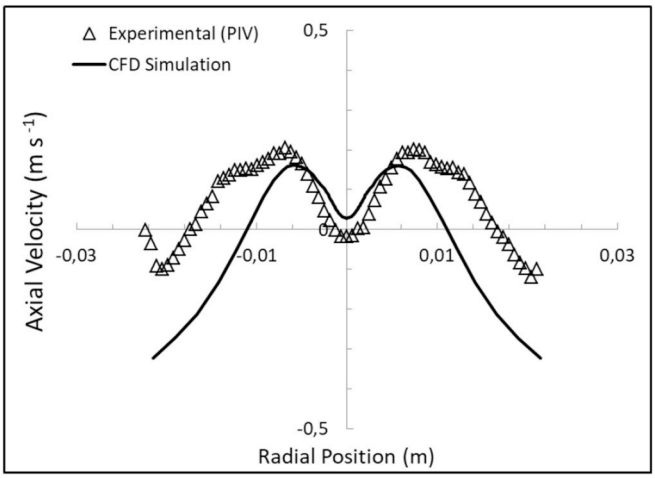

(a)

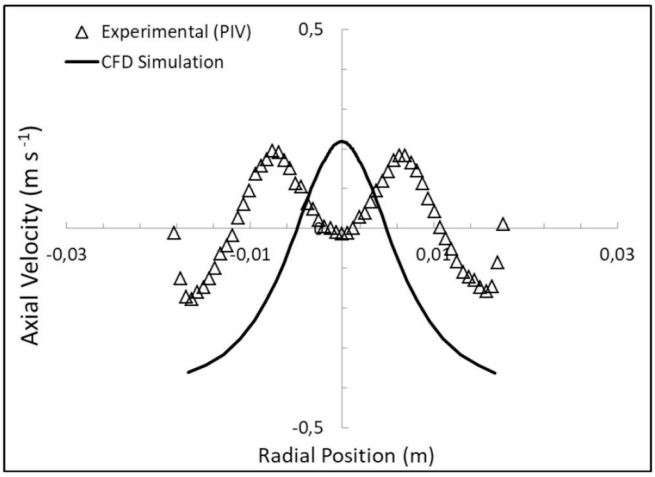

(b)

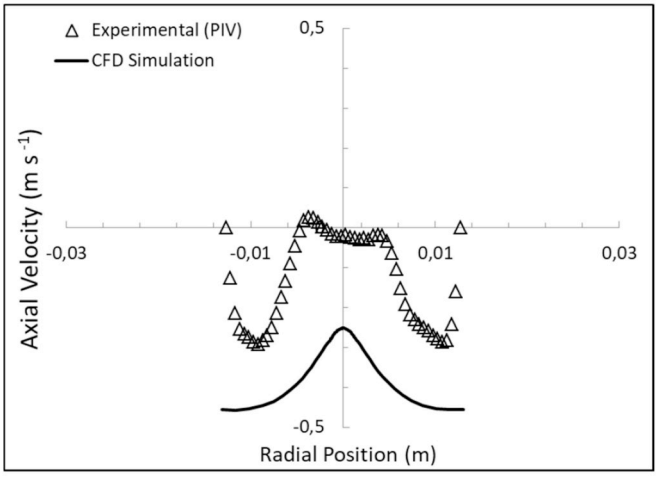

(c)

Fig. 8. Axial velocity profiles from experiments and CFD simulations at (a) Station 1, (b) Station 2 and (c) Station 3.

the vortex finder is one of the parameters which influences the appearance of these shapes.

Low velocities around the centerline of the hydrocyclone were also confirmed by observation *in locus* at the time of the experiments. The low pressure zone along the central axis caused the appearance of some micro-bubbles, which come probably from air dissolved in water. It could be noted that these micro-bubbles migrated to the overflow tube with very low velocities, confirming the experimental profile provided by the PIV. The CFD simulations did not considered air as a third dispersed phase, so they would never predict such phenomenon.

From Fig. 8, it can be thus concluded that CFD simulations could not capture axial velocity profiles properly. Besides the different shapes (inverted "V" or "W"), the magnitude of the axial velocity as well as the width of the core region (where the axial velocity changes sign) are significantly different for CFD and PIV. It is well known how complex is the flow field inside a hydrocyclone and turbulence models are not yet accurate enough to capture reliably its velocity field. It should be stressed though that the axial velocity is smaller in magnitude and much less important in the separation process associated with particle terminal velocity than the tangential velocity. Therefore, although the axial velocity profiles obtained with CFD simulations are not close to those observed experimentally, it does not invalidate the overall CFD results, such as separation efficiency and flow ratio, as can be seen in the results of the next section.

3.3. Oil-water experiments: separation efficiencies and flow ratios

Fig. 9 shows an image of the 40% (v/v) oil-water mixture being separated within the hydrocyclone HC-12. The whitish region in the overflow represents the high oil concentration zone while it can be seen how free of oil the underflow is. Oil concentrations have been measured at inlet, overflow and underflow streams.

Table 5 presents the results for the triplet of experiments conducted to measure separation efficiency and flow ratio. It can be seen that the experiments showed good reproducibility and average values with low deviations. The hydrocyclone designed has provided total efficiency of $E_T = 93\%$ with a small flow ratio of $R_F = 7\%$ which implied reduced total efficiency being $E'_T \cong E_T = 93\%$. It can be noted that for an inlet stream with 40% oil-in-water concentration, the overflow and underflow oil concentrations are 89% and 4% respectively, which shows the high efficiency achieved.

Values of R_{FT} are concordant in both Tables 3 and 5, showing good agreement between numerical and experimental results. Tables 3 and 5 also allows comparison of R_F values. The difference between numerical and experimental results is large in percentage, but small in absolute value. Such difference has thus been considered acceptable.

In order to compare computational and experimental reduced total efficiency and analyze possible droplet breakup and coalescence, the cumulative distributions at inlet, overflow and underflow are needed. These curves have been obtained experimentally with an FBRM and are presented in Fig. 10. It can be confirmed that the coarser distribution belongs to the overflow stream, what is expected, since this is the oil-rich stream (around 90%).

The inlet droplet diameter distribution in Fig. 10 has been used to determine the parameters of Equation (9), resulting in Equation (33) with a coefficient of determination $R^2 = 0.9941$.

$$y = 1 - \exp\left[- \left(\frac{d}{241} \right)^{1.86} \right] \tag{33}$$

In order to estimate the reduced total efficiency E'_T based on computational results, Equation (33) has been substituted into Equation (32), which has been integrated according to Equation (10). The computational reduced total efficiency obtained was $E'_T = 93.3\%$ which is the same as that obtained experimentally, as shown in Table 5. This validates the computational results, showing that the physical modeling of the simulations was adequate.

It is curious though that such exact match has been achieved, since the physical modeling has been simplified, as a first approach, not to account for breakup and coalescence models.

Breakup and coalescence can be analyzed by reconstituting the inlet cumulative undersize distribution through Equation (10), with the measured total efficiency (0.93 from Table 5) and the overflow and underflow cumulative undersize distributions, presented in Fig. 10.

Fig. 11 shows both experimental and calculated (Equation (10)) inlet cumulative undersize distribution. It can be seen that both curves are very close up to a diameter of 150 μm, which means that, for droplets up to this size, none or very little breakup has occurred. For higher droplet sizes, Fig. 11 shows that some coalescence has occurred, since the calculated inlet cumulative undersize distribution is coarser than that measured experimentally at inlet. According to Fig. 5, droplets with a diameter higher than 125 μm are collected with 100% efficiency and therefore, for such inlet cumulative size distribution, no coalescence or breakup models are needed. This indicates that previous analysis about the relevance of the near-centerline velocity profiles (Fig. 7) is pertinent.

It must be stressed that mature oil fields are often subjected to EOR (Enhanced Oil Recovery) and the chemicals used, such as polymers, may improve oil-water stabilization, as noted by Wang et al. (2019). This may affect oil dr size distribution and tendency to droplet coalescence. The latter may improve separation efficiency in hydrocyclones, though.

At last, Fig. 12 shows the influence of global flow ratio on total efficiency. It can be said that total efficiency increases linearly with global flow ratio, according to Equation (34), which presented a coefficient of determination of $R^2 = 0.989$.

$$E_T = 2.19 R_{FT} + 2.26 \tag{34}$$

It must be stressed that this linear relation applies only for the range tested, since total efficiency tends to 100% as global flow ratio tends to 100%.

4. Conclusions

The hydrocyclone developed in the present work separates a 40% oil-

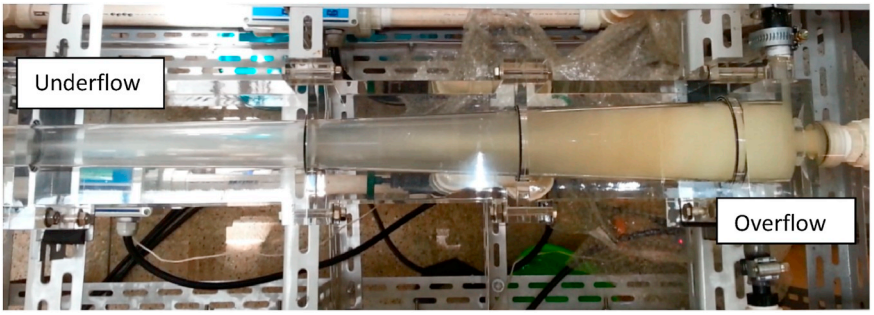

Fig. 9. Oil fraction inside the HC-12.

Table 5
Total efficiency and flow ratios from experiments with the same operating conditions as the biphasic CFD simulation.

Exp.	Q_t (l/min)	Q_{ovf} (l/min)	Q_{und} (l/min)	$C_{v\ (inlet)}$	$C_{v\ (ovf)}$	$C_{v\ (und)}$	R_{FT}	R_F	ET	ET′
1	21.30	8.93	12.36	0.40	0.89	0.05	0.42	0.06	0.93	0.93
2	20.77	9.11	11.66	0.39	0.87	0.03	0.43	0.09	0.95	0.95
3	20.73	7.48	13.25	0.40	0.90	0.05	0.41	0.06	0.92	0.91
Avg.	20.93 ± 0.37	8.51 ± 1.03	12.42 ± 0.83	0.40 ± 0.01	0.89 ± 0.02	0.04 ± 0.01	0.42 ± 0.01	0.07 ± 0.02	0.93 ± 0.02	0.93 ± 0.02

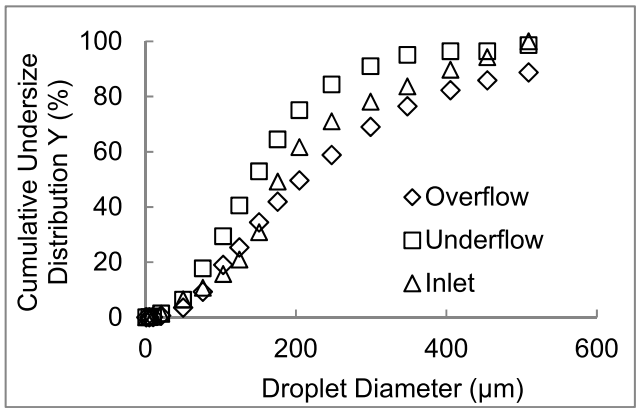

Fig. 10. Cumulative distribution of oil droplet sizes at inlet, underflow and overflow streams.

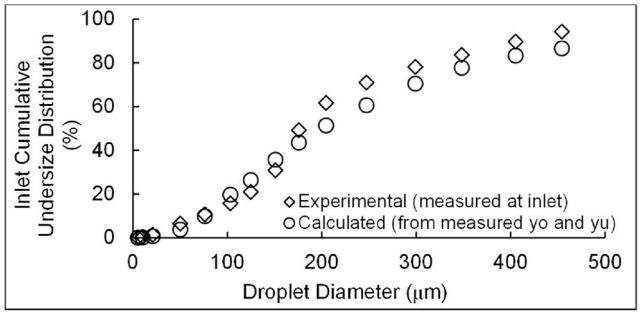

Fig. 11. Calculated and experimental reduced grade efficiencies for the hydrocyclone HC-12.

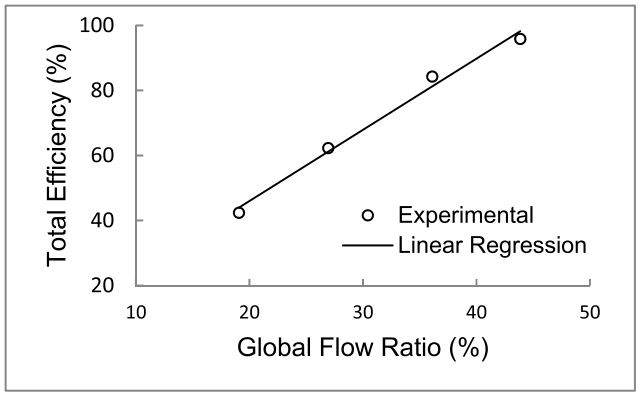

Fig. 12. Experimental total efficiency as a function of global flow ratio.

in-water concentration stream with 93% ± 2% efficiency. Besides such high inlet oil concentration being unprecedented, high efficiencies, also not often reported in the literature, have been achieved. This makes it an interesting alternative to be considered in mature oil fields. Therefore the present work strongly suggests the replacement of production separators by hydrocyclones, such as those designed here, specially for subsea facilities, since they have been proven viable.

It has been shown that simulations can be performed in steady state and that the turbulence model used did not return close match to experimental velocity profiles. It has been discussed, though, that this probably does not affect the prediction of total separation efficiency. Tangential velocity profiles near the central axis are expected to play the important role for oil-water separation and, in this region, numerical simulations returned reasonably good predictions when compared to experimental data. Axial velocity profiles have not been well captured by simulation either, however this velocity component is not expected to affect significantly the physical separation process.

Numerical simulation have been validated by comparing experimental reduced total efficiency with that predicted by CFD simulations for the same inlet cumulative undersize distribution. Taking into account experimental error of 2%, the same computational and experimental reduced total efficiencies of 93% has been found.

A methodology to analyze the effect of droplet breakup and coalescence, using measured inlet, overflow and underflow cumulative size distribution, has been presented. It has been shown that for the inlet cumulative undersize distribution used, breakup was negligible and coalescence occurred only for droplet diameters higher than that separated with 100% grade efficiency.

The experimental characterization of the system has validated the methodology used to design a high-efficiency hydrocyclone for high inlet oil concentrations, such as 40%.

Acknowledgements

The authors acknowledge the Computational Fluid Dynamics Laboratory (LabCFD), the Interdisciplinary Center of Fluid Dynamics (NIDF), both located at UFRJ campus, and the Giulio Massarani Fluid Flow Laboratory (LEF), at UFRRJ campus, by extensive collaboration in this work. JBRL benefited from a CNPq Research Fellowship (Grant No 309455/2016-2) and from further financial support through Grants CNPq 439255/2018-0 and FAPERJ E-26/203.257/2016.

Appendix A. Supplementary data

Supplementary data to this article can be found online at https://doi.org/10.1016/j.petrol.2019.106788.

Nomenclature

Roman Symbols

C	stands for the continuous phase (particles – droplets)
C_D	drag coefficient
$C_{v\ (inlet)}$	oil concentration at inlet;
$C_{v\ (ovf)}$	oil concentration at overflow
$C_{v\ (und)}$	oil concentration at underflow
D	normal distance to the wall (equations (26) and (27)); particle diameter
D	diameter between the first and second conical parts
D_{ij}	total diffusion term
Dc	cylindrical part diameter
Di	inlet diameter
Do	overflow diameter
d_P	droplet (or particle) diameter
Du	underflow diameter
d'_{50}	droplet (or particle) size at 50% reduced efficiency
E_T	total efficiency
E'_T	reduced efficiency
f	drag function
G	grade efficiency
G'	reduced grade efficiency
K	turbulent kinetic energy; Rosin-Rammler model parameter (equation (9))
K_{pq}	interphase momentum exchange coefficient
L1	length of hydrocyclone cylindrical part
M	mixture properties and mixture velocities
m	Rosin-Rammler model parameter
n	parameter of grade efficiency equation
n_k	component of the unit normal to the wall
P_{ij}	stress production term
p	static pressure
p	dispersed phase (particles - droplets)
q	stands for the qth phase
Q_a	water volumetric flow rate at inlet;
Q_o	oil volumetric flow rate at inlet;
Q_{ovf}	overflow flow rate
Q_t	total flow rate (oil + water)
Q_{und}	underflow flow rate
$\tilde{R}_{ij}$	phase-average Reynolds stress tensor
R_F	flow ratio
R_{FT}	global flow ratio (or overflow-to-throughput ratio)
U	velocity vector
VF	vortex finder length
x_k	component of the unit normal to the wall
W_{ac}	water mass flow at concentrated stream (overflow)
W_a	water mass flow at feed stream (inlets)
W_d	mass flow of particles with size d in the feed stream
W_{dc}	mass flow of particles (or droplet) with size d in the concentrate stream
y	cumulative undersize distribution

Greek Letters

α	volume fraction
ε	viscous dissipation rate
ε_{ij}	viscous dissipation term
Φ	generic variable
φ_{ij}	pressure strain term
$\varphi_{ij,1}$	slow pressure strain term
$\varphi_{ij,2}$	the rapid pressure strain term
$\varphi_{ij,w1}$ *and* $\varphi_{ij,w2}$	wall reflection terms
Γ	generic property
Θ_1	angle of the first conical section of hydrocyclone
Θ_2	angle of the second conical section of hydrocyclone

ρ	fluid density
μ	fluid viscosity
μ_t	turbulent viscosity
τ	stress-strain tensor
$\tilde{\tau}_q$	the total phase-average stress-strain tensor of phase q
Λ	wavelength

Subscripts

C	continuous phase
m	mixture
o	related to overflow stream
p	particle
q	qth phase
u	related to underflow stream

Acronyms

CFD	Computational Fluid Dynamics
FBRM	Focused Beam Reflectance Measurement
PIV	Particle Image Velocimetry

References

Adrian, R.J., 1997. Dynamic ranges of velocity and spatial resolution of particle image velocimetry. Meas. Sci. Instrum. 8, 1393–1398.

Altieri, G., Genovese, F., Tauriello, A., Di Renzo, G.C., 2015. Innovative plant for the separation of high quality virgin olive oil (VOO) at industrial scale. J. Food Eng. 166, 325–334. https://doi.org/10.1016/J.JFOODENG.2015.06.033.

ANSYS Fluent, 2010. 13 Theory Guide. ANSYS Inc.

ANSYS Meshing, 2010. 13 User's Guide. ANSYS Inc.

Antunes, M., Medronho, R., 1992. Bradley hydrocyclones: design and performance analysis. In: Svarovsky, L., Thew, M. (Eds.), Hydrocyclones: Analysis and Applications. Kluwer Academic Publishers.

Bai, Z., Wang, H., Tu, S., 2011. Oil-water separation using hydrocyclones enhanced by air bubbles. Chem. Eng. Res. Des. 89, 55–59. https://doi.org/10.1016/j.cherd.2010.04.012.

Bhaskar, K.U., Murthy, Y.R., Raju, M.R., Tiwari, S., Srivastava, J.K., Ramakrishnan, N., 2007. CFD simulation and experimental validation studies on hydrocyclone. Min. Eng. 20, 60–71. https://doi.org/10.1016/j.mineng.2006.04.012.

Braga, E.R., Huziwara, W.K., Martignoni, W.P., Scheid, C.M., Medronho, R.A., 2015. Improving hydrocyclone geometry for oil/water separation. Braz. J. Pet. Gas. 9, 115–123.

Bretney, E., 1891. U.S. Patent No. 453, 105.

Cao, Y., Jin, Y., Li, J., Zou, D., Chen, X., 2016. Demulsification of the phosphoric acid-tributyl phosphate (W/O) emulsion by hydrocyclone. Separ. Purif. Technol. 158, 387–395. https://doi.org/10.1016/j.seppur.2015.12.038.

Castilho, L.R., Medronho, R.A., 2000. Simple procedure for design and performance prediction of Bradley and Rietema hydrocyclones. Min. Eng. 13, 183–191. https://doi.org/10.1016/S0892-6875(99)00164-8.

Coelho, M.A.Z., Medronho, R.A., 2001. A model for performance prediction of hydrocyclones. Chem. Eng. J. 84, 7–14. https://doi.org/10.1016/S1385-8947(00)00265-5.

Coleman, H.W., Steele, W.G., 2009. Experimentation, Validation and Uncertainty Analysis for Engineers. John Wiley & Sons.

Dlamini, M.F., Powell, M.S., Meyer, C.J., 2005. A CFD simulation of a single phase hydrocyclone flow field. J. South Afr. Inst. Min. Metall. 105, 711–717.

Elsayed, K., Lacor, C., 2010. Application of response surface methodology for modeling and optimization of the cyclone separator for minimum pressure drop. In: V European Conference on Computational Fluid Dynamics, 14-17 June, Lisbon.

Gibson, M.M., Launder, B.E., 1978. Ground effects on pressure fluctuations in the atmospheric boundary layer. J. Fluid Mech. 86, 491–511.

Hamza, J.E., Al-Kayiem, H.H., Lemma, T.A., 2019. Experimental investigation of the separation performance of oil/water mixture by compact conical axial hydrocyclone. Therm. Sci. Eng. Prog. https://doi.org/10.1016/j.tsep.2019.100358 (in press).

Harasek, M., Horvath, A., Jordan, C., 2008. Influence of vortex finder diameter on axial gas flow in simple cyclone. Chem. Prod. Process Model. 3 (1) https://doi.org/10.2202/1934-2659.1149.

Huang, L., Deng, S., Chen, M., Guan, J., 2017. Numerical simulation and experimental study on a deoiling rotary hydrocyclone. Chem. Eng. Sci. 172, 107–116. https://doi.org/10.1016/j.ces.2017.06.030.

Huang, L., Deng, S., Guan, J., Chen, M., Hua, W., 2018. Development of a novel high-efficiency dynamic hydrocyclone for oil–water separation. Chem. Eng. Res. Des. 130, 266–273. https://doi.org/10.1016/j.cherd.2017.12.030.

Kelsall, D.F., 1952. A study of the motion of solid particles in a hydraulic cyclone. Trans. Inst. Chem. Eng. 30, 87–108.

Liu, L., Zhao, L., Yang, X., Wang, Y., Xu, B., Liang, B., 2019. Innovative design and study of an oil-water coupling separation magnetic hydrocyclone. Separ. Purif. Technol. 213, 389–400. https://doi.org/10.1016/j.seppur.2018.12.051.

Liu, S., Yan, Y., Gao, Y., 2018. Optimization of geometry parameters with separation efficiency and flow split ratio for downhole oil-water hydrocyclone. Therm. Sci. Eng. Prog. 8, 370–374. https://doi.org/10.1016/j.tsep.2018.08.011.

Liu, Y., Wang, H., Xu, Y., Fang, Y., Chen, X., 2017. Sludge disintegration using a hydrocyclone to improve biological nutrient removal and reduce excess sludge. Separ. Purif. Technol. 177, 192–199. https://doi.org/10.1016/j.seppur.2016.11.001.

Marins, L.P.M., Duarte, D.G., Loureiro, J.B.R., Moraes, C.A.C., Freire, A.P.S., 2010. LDA and PIV characterization of the flow in a hydrocyclone without an air-core. J. Pet. Sci. Eng. 70, 168–176. https://doi.org/10.1016/j.petrol.2009.11.006.

Medronho, R.A., Svarovsky, L., 1984. Tests to verify hydrocyclones scale-up procedures. In: 2nd Int. Conference on Hydrocyclones, pp. 1–14.

Motin, A., Tarabara, V.V., Petty, C.A., Bénard, A., 2017. Hydrodynamics within flooded hydrocyclones during excursion in the feed rate: understanding of turndown ratio. Separ. Purif. Technol. 185, 41–53.

Murthy, Y.R., Bhaskar, K.U., 2012. Parametric CFD studies on hydrocyclone. Powder Technol. 230, 36–47. https://doi.org/10.1016/j.powtec.2012.06.048.

Ni, L., Tian, J., Shen, C., Zhao, J., 2016. Experimental study of the separation performance of a novel sewage hydrocyclone used in sewage source heat pump. Appl. Therm. Eng. 106, 1300–1310. https://doi.org/10.1016/j.applthermaleng.2016.06.093.

Noroozi, S., Hashemabadi, S.H., 2011. CFD analysis of inlet chamber body profile effects on de-oiling hydrocyclone efficiency. Chem. Eng. Res. Des. 89, 968–977.

Obeng, D.P., Morrell, S., Napier-Munn, T.J., 2005. Application of central composite rotatable design to modelling the effect of some operating variables on the performance of the three-product cyclone. Int. J. Miner. Process. 76, 181–192. https://doi.org/10.1016/j.minpro.2005.01.002.

Plitt, L.R., 1976. A mathematical model of the hydrocyclone classifier. Cim. Bull. 114–123.

Rocha, A.D., Bannwart, A.C., Ganzarolli, M.M., 2017. Effects of inlet boundary conditions in an axial hydrocyclone. J. Braz. Soc. Mech. Sci. 39 (9), 3425–3437.

Rosin, P., Rammler, E., 1933. The laws governing the fineness of powdered coal. J. Inst. Coal. 7, 29–36.

Saidi, M., Maddahian, R., Farhanieh, B., Afshin, H., 2012. Modeling of flow field and separation efficiency of a deoiling hydrocyclone using large eddy simulation. Int. J. Miner. Process. 112 (113), 84–93. https://doi.org/10.1016/j.minpro.2012.06.002.

Schiller, L., Naumann, A., 1935. A drag coefficient correlation. Z. Des Ver. Deutsch. Ing. 77, 318–320.

Schütz, S., Gorbach, G., Piesche, M., 2009. Modeling fluid behavior and droplet interactions during liquid-liquid separation in hydrocyclones. Chem. Eng. Sci. 64, 3935–3952. https://doi.org/10.1016/j.ces.2009.04.046.

Slack, M.D., Del Porte, S., Engelman, M.S., 2004. Designing automated computational fluid dynamics modelling tools for hydrocyclone design. Miner. Eng. 17, 705–711. https://doi.org/10.1016/j.mineng.2003.12.009.

Swain, S., Mohanty, S., 2013. A 3-dimensional Eulerian-Eulerian CFD simulation of a hydrocyclone. Appl. Math. Model. 37, 2921–2932. https://doi.org/10.1016/j.apm.2012.06.007.

Wang, C., Wu, R., 2018. Experimental and simulation of a novel hydrocyclone-tubular membrane as overflow pipe. Separ. Purif. Technol. 198, 60–67. https://doi.org/10.1016/J.SEPPUR.2017.04.034.

Wang, Z., Lin, X., Yu, T., Zhou, N., Zhong, H., Zhu, J., 2019. Formation and rupture mechanisms of visco-elastic interfacial films in polymer stabilized emulsions. J. Dispersion Sci. Technol. 40 (4), 612–626. https://doi.org/10.1080/01932691.2018.1478303.

Young, G.A.B., Wakley, W.D., Taggart, D.L., Andrews, S.L., Worrell, J.R., 1994. Oil-water separation using hydrocyclones: an experimental search for optimum dimensions. J. Pet. Sci. Eng. 11, 37–50. https://doi.org/10.1016/0920-4105(94)90061-2.

Zhang, C., Wei, D., Cui, B., Li, T., Luo, N., 2017. Effects of curvature radius on separation behaviors of the hydrocyclone with a tangent-circle inlet. Powder Technol. 305, 156–165. https://doi.org/10.1016/j.powtec.2016.10.002.

Zhen-bo, W., Yi, M., You-hai, J., 2011. Simulation and experiment of flow field in axial-flow hydrocyclone. Chem. Eng. Res. Des. 89, 603–610. https://doi.org/10.1016/j.cherd.2010.09.004.

Zhou, N., Gao, Y., An, W., Yang, M., 2010. Investigation of velocity field and oil distribution in an oil-water hydrocyclone using a particle dynamics analyzer. Chem. Eng. J. 157, 73–79. https://doi.org/10.1016/j.cej.2009.10.049.